Macroscopic effects of inter and intra particle dynamics on vehicle mobility using nonlocal particle based modeling

Debdeep Bhattacharya
University of Utah
Department of Mathematics
Salt Lake City, Utah, USA
Email: d.bhattacharya@utah.edu

Robert P. Lipton
Louisiana State University
Department of Mathematics
Baton Rouge, Louisiana, USA
Email: lipton@lsu.edu

A nonlocal particle-based computational platform based on the coupling of peridynamics and discrete element method (PeriDEM) is introduced for the simulation of a vehicle wheel rolling over gravel beds, where various gravel particle geometry, topology, deformablity, and fracture toughness are accommodated. Comparison of dynamic vehicle mobility measures including longitudinal displacement, velocity, and slip for transit over particle beds consisting of different gravel geometries and topologies are carried out. The effect of gravel shape on the horizontal displacement, velocity, and slip of the wheel is investigated through numerical simulation. The effect of gravel particle geometry on the overall energy needed to travel a prescribed distance is investigated. Particle geometry and topology affects particle damage, and consequently influences macroscopic transport properties. Our simulations show that the driving torque exhibits a monotonically increasing trend with increasing slip and follows the trend seen in experiments.

1 INTRODUCTION

Despite poor driving conditions and strength relative to other surfaces, gravel roads remain a go to choice for constructing roadways and pavements, due to low construction cost [1, 2]. Road quality factors such as water absorption, abrasion, [3] washboard formation [4], as well as dynamic vehicle mobility response including comfort, handling, and degradation of vehicle machinery [5] are affected by the choice of gravel [6]. Recent studies have shown that [7, 8, 9] gravel geometry plays an important role in compression and shear strength, and the stability of gravel aggregates. Interlocking behavior, which is more prominent in angular particles, is shown to correlate with higher shear strength [10]. Gravel form, angularity, and surface textures are found to affect the crushing in aggregates via jaw and cone crushing experiments [3]. Therefore, gravel lithology, geometry, size distribution, and arrangement play an important role in vehicle mobility on gravel roads. Improved understanding of the dependence of vehicle mobility on gravel properties can aid advanced geotechnical exploration techniques such as the mobility of Mars Exploration Rover on martian regolith [11].

Traditional approaches to study vehicle mobility on gravel aggregates rely on the discrete element method (DEM) simulations, where each gravel particle boundary is considered to be rigid [12]. While traditional DEM-based approaches capture the rigid motion of the boundary of each gravel particle, but they do not account for the deformation of individual gravel particles. In addition, traditional DEM does not fully capture complex damage propagation based on each particle's geometry, nor the effects of notched or pre-cracked particles. Hence any capability of capturing elastic and inelastic deformation of individual particle will lead to improved models for granular media. More recent work accounts for particle shapes and particle fracture using new enhanced DEM methods, see [13, 14].

In this treatment we depart from DEM and model elastic as well as extreme intra-particle deformation using a nonlocal continuum formulation. We follow a peridynamic modelng approach developed in [15]. In this modeling approach both elastic deformation and fracture are coupled implicitly and evolve autonomously. Using this model the intra-particle deformation can exhibit extreme deformation resulting in fracture. Peridyamic models have been used recently for mesoscale modeling of granular media, especially for capturing elastic and inelastic deformation and intra-granular force within individual grains. Behzadinasab et. al. [16] studied shockwave decay in particle beds of circular particles. Zhu and Zhao [17, 18] used a Weibull statistics-peridynamics approach to investigate crushing piles of sand. In recent joint work the authors combined the direct element method (DEM) with peridynamics (PeriDEM) to the study of granular flows, Jha et. al. [19].

Earlier studies have shown that particle geometry plays an important role in determining the mechanical response of the aggregate. Studies on force chains and interlocking particle columns [20] have demonstrated the strength of aggregates with relatively relatively high interstitial volume fraction. Since vehicle mobility is directly affected by the mechanical response of the gravel bed, high-fidelity grain-scale simulations of gravel aggregates plays an important role in the study of off-road mobility of wheeled vehicles. While Finite Element Method (FEM) and DEM-based approaches were used to model the deformation of the wheel [21] and plasticity of the terrain [22], the macroscopic effect of individual grain shape, deformability, and damage have not been investigated in the literature. The goal of this paper is to apply a high-fidelity simulation platform [23] to link the geometric effects of individual particle grains to the vehicle mobility over gravel pavement. Our method is quite general and even allows us to explore the effect of hollow grains. These grains can comminute when the weight of the wheel is put on the aggregate, leading to significant sinkage, see Section 4.

The paper proceeds with a description of the dynamic model given in section 2. This is followed by a description of the main points of the numerical implementation provided in section 3. The core of the paper consists of the numerical experiments and the identification of the macroscopic effect of gravel particle shapes and topology on roadbed performance carried out in section 4. The conclusions are summarized in section 5.

2 MODELING

Our nonlocal modeling approach tracks both elastic and inelastic deformation inside a particle as a field theory that is nonlocal both in space and time. In the reference configuration, each gravel particle as well as the wheel is denoted by a domain in $\mathbb{R}^2$. The intraparticle force acting on a point $\mathbf{x}$ inside the i^{th} particle domain $D_i \in \mathbb{R}^2$ is given by the integro-differential equation

$$\boldsymbol{F}_i^{int}(\mathbf{x}, \mathbf{u}; t) = \int\limits_{H_\epsilon(\mathbf{x}) \cap D_i} \mathbf{f}(\mathbf{u}(\mathbf{x}', t), \mathbf{u}(\mathbf{x}, t), \mathbf{x}', \mathbf{x}, t) dV_{\mathbf{x}'}, \tag{1}$$

where $\mathbf{f}$ is the pairwise force density function. The length scale ϵ over which lonlocal interaction is possible is called the *horizon*. The neighborhood of a point $\mathbf{x}$ is the set $H_\epsilon(\mathbf{x}) = \{\mathbf{x}' \in \mathbb{R}^2 : |\mathbf{x}' - \mathbf{x}| \leq \epsilon\}$. For a material point $\mathbf{x}' \in H_\epsilon(\mathbf{x}) \cap D$, $V_{\mathbf{x}'}$ denotes the volume element associated with $\mathbf{x}'$. Here the force density has the unit of force per area squared. Next, we describe the constitutive law relating force density to strain. Here the force density is given for two-point interactions. This is called bond-based peridynamics [15]. Given $\mathbf{x} \in D$ and $\mathbf{x}' \in H_\epsilon(\mathbf{x})$, the vector $\boldsymbol{\xi} = \mathbf{x}' - \mathbf{x}$ is referred to as a *bond*. Defining $\boldsymbol{\eta} = \mathbf{u}(\mathbf{x}', t) - \mathbf{u}(\mathbf{x}, t)$, the *stretch* s associated with a bond $\boldsymbol{\xi}$ is defined as $s = s(\mathbf{u}(\mathbf{x}', t), \mathbf{u}(\mathbf{x}, t), \mathbf{x}', \mathbf{x}) := \frac{|\boldsymbol{\xi}+\boldsymbol{\eta}| - |\boldsymbol{\xi}|}{|\boldsymbol{\xi}|}$.

We consider the microelastic model introduced in [24], where the pairwise force density function $\mathbf{f}$ is given by

$$\mathbf{f} = \begin{cases} c_w \; w(|\boldsymbol{\xi}|) \; s \; \frac{\boldsymbol{\xi}+\boldsymbol{\eta}}{|\boldsymbol{\xi}+\boldsymbol{\eta}|} & \text{if } |\boldsymbol{\xi}| < \epsilon \\ 0 & \text{otherwise,} \end{cases} \tag{2}$$

where the *micromodulus function* $w(r)$ is a non-negative scalar function that is non-increasing in r. The peridynamic spring constant c_w is chosen such that the integral operator agrees with the Cauchy-Navier operator up to the second order. We list the value of the peridynamic spring constant and two micromodulus functions in Table 1.

2.1 Irreversible damage and memory

In the prototype microelastic brittle (PMB) material model [25], the bond $\boldsymbol{\xi}$ between $\mathbf{x}$ and $\mathbf{x}'$ are broken at time t if the stretch $s(\mathbf{u}(\mathbf{x}', t), \mathbf{u}(\mathbf{x}, t), \mathbf{x}', \mathbf{x})$ exceeds the *critical stretch* s_0 in the absolute value, i.e. when $|s| > |s_0|$. The value of s_0 is determined by equating the critical energy release rate G_c with the total energy required to sever all bonds across a crack surface of unit area. In table 1, we list the value of the critical stretch for both "constant" and "conic" micromodulus functions [26]. Once a bond is broken at time $t = t_0$, it remains broken for all time $t > t_0$. The *damage* of a material point $\mathbf{x}$ is defined as the ratio of the number of intact bonds connected to $\mathbf{x}$ at time t to the number of bonds connected to $\mathbf{x}$ in the reference configuration (i.e. at $t = 0$).

Table 1: Peridynamic spring constant for various choices the micromolulus function in eq. (2).

Type	$c_w w(\|\boldsymbol{\xi}\|)$	s_0
Constant	$\frac{6E}{\pi\epsilon^3(1-\nu)}$	$\sqrt{\frac{4\pi G_c}{9E\epsilon}}$
Conic	$\frac{24E}{\pi\epsilon^4(1-\nu)}(\epsilon - \|\boldsymbol{\xi}\|)$	$\sqrt{\frac{5\pi G_c}{9E\epsilon}}$

Because bond-based peridynamics is a two-point interaction model the Poisson ratio is $\frac{1}{3}$ in 2D and $\frac{1}{4}$ in 3D [27]. While this limitation can be easily overcome by using a state-based model [28], but we do not pursue that here.

In the following section we introduce the different interparticle forces and wall forces then combine them with Equation (1) to get the equation of evolution for every particle in the aggregate given in Section 2.2.6.

2.2 Contact model

To capture the inter grain interactions we apply the short-range contact force model used by [25], [16], and [23]. In the short-range contact model, two material points belonging to two different peridynamic domains are said to be in contact if they are within a certain distance R_c, called the *contact radius*. Let D_1 and D_2 be two particles and with $\mathbf{x} \in D_1$ and $\mathbf{y} \in D_2$. Define the positions $\mathbf{p}(\mathbf{x},t) = \mathbf{x}+\mathbf{u}(\mathbf{x},t)$ and $\mathbf{p}(\mathbf{y},t) = \mathbf{y}+\mathbf{u}(\mathbf{y},t)$. We define the *normal direction* $\mathbf{e}(\mathbf{y},\mathbf{x},t)$ by the unit vector $\mathbf{e}(\mathbf{y},\mathbf{x},t) = \frac{\mathbf{p}(\mathbf{y},t)-\mathbf{p}(\mathbf{x},t)}{|\mathbf{p}(\mathbf{y},t)-\mathbf{p}(\mathbf{x},y)|}$ the denotes the direction from $\mathbf{x}$ to $\mathbf{y}$.

2.2.1 *Repulsive contact force*

The short-range repulsive force $\mathbf{f}_r(\mathbf{y},\mathbf{x},t)$ exerted on $\mathbf{x} \in D_1$ by $\mathbf{y} \in D_2$ (see [25, 16, 19]) is given by

$$\mathbf{F}_r(\mathbf{y},\mathbf{x},t) = \begin{cases} -K_n(R_c - |\mathbf{p}(\mathbf{y},t)-\mathbf{p}(\mathbf{x},t)|)V_{\mathbf{x}}V_{\mathbf{y}}\mathbf{e}(\mathbf{y},\mathbf{x},t), \\ \qquad \text{if } |\mathbf{p}(\mathbf{y},t)-\mathbf{p}(\mathbf{x},t)| < R_c \\ 0, \quad \text{otherwise} \end{cases} \tag{3}$$

where the normal contact stiffness is $K_n = \frac{18k}{\pi\epsilon^5}$, where k is the bulk modulus, $V_{\mathbf{x}}$ and $V_{\mathbf{y}}$ are volume elements associated with $\mathbf{x}$ and $\mathbf{y}$, respectively [16, 19]. When the participating peridynamic bodies have bulk moduli $k_1 \neq k_2$, an effective bulk modulus is used and given by the harmonic mean $k = \frac{2k_1k_2}{k_1+k_2}$ [19]. Although the repulsive force is chosen to be linear in the distance between the points in contact, one can consider a nonlinear relation, but over short distances they are comparable [29].

2.2.2 *Tangential friction force*

In addition to exchanges of momentum, peridynamic domains also slide against each other. Therefore, dissipation of energy via friction forces is an essential component of interparticle interaction. Interparticle friction is incorporated using Coulomb's law. The friction force $\mathbf{f}_f(\mathbf{y},\mathbf{x},t)$ acts in the direction perpendicular to $\mathbf{e}(\mathbf{y},\mathbf{x},t)$. Let the relative velocity of $\mathbf{y} \in D_2$ with respect to $\mathbf{x} \in D_1$ be denoted by $\mathbf{v}(\mathbf{y},\mathbf{x},t) := \dot{\mathbf{u}}(\mathbf{y},t) - \dot{\mathbf{u}}(\mathbf{x},t)$. The component of $\mathbf{v}$ perpendicular to $\mathbf{e}$ is given by $\mathbf{v}_\perp(\mathbf{y},\mathbf{x},t) = \mathbf{v}(\mathbf{y},\mathbf{x},t) - (\mathbf{v}(\mathbf{y},\mathbf{x},t)\cdot\mathbf{e}(\mathbf{y},\mathbf{x},t))\,\mathbf{e}(\mathbf{y},\mathbf{x},t)$. Now, define the *tangential direction* $\mathbf{e}_\perp(\mathbf{y},\mathbf{x},t)$ by $\mathbf{e}_\perp(\mathbf{y},\mathbf{x},t) = \frac{\mathbf{v}_\perp(\mathbf{y},\mathbf{x},t)}{|\mathbf{v}_\perp(\mathbf{y},\mathbf{x},t)|}$. Note that $\mathbf{e}_\perp \in \{\mathbf{u}\in\mathbb{R}^2 : \mathbf{e}\cdot\mathbf{u} = 0\}$ and $\mathbf{e}_\perp$ lies on the plane spanned by the vectors $\mathbf{e}$ and $\mathbf{v}$.

To capture the stick/slip transition between the static and kinetic regimes, we use the regularized friction model [30, 31]. Therefore, the tangential friction force is given by

$$\mathbf{F}_f(\mathbf{y},\mathbf{x},t) = \tag{4}$$

$$\begin{cases} -\mu\,|\mathbf{F}_r(\mathbf{y},\mathbf{x},t)|\,\mathbf{e}_\perp(\mathbf{y},\mathbf{x},t), \\ \qquad \text{if } |\mathbf{v}_\perp(\mathbf{x},\mathbf{y},t)| > v_{\text{thr}}(\mathbf{x},\mathbf{y},t,\Delta t) \\ -\frac{1}{\epsilon_f}\,|\mathbf{v}_\perp(\mathbf{x},\mathbf{y},t)|\,\mathbf{e}_\perp(\mathbf{y},\mathbf{x},t), \\ \quad \text{if } 0 \le |\mathbf{v}_\perp(\mathbf{x},\mathbf{y},t)| \le v_{\text{thr}}(\mathbf{x},\mathbf{y},t,\Delta t), \end{cases} \tag{5}$$

where ϵ_f is a regularization parameter given by $\epsilon_f = \frac{\Delta t}{\rho V_{\mathbf{x}}}$, where Δt is the numerical time step. Here, ϵ_f is chosen so that once $0 \le |\mathbf{v}_\perp(\mathbf{x},\mathbf{y},t)| \le v_{\text{thr}}(\mathbf{x},\mathbf{y},t,\Delta t)$, the relative velocity of $\mathbf{p}(\mathbf{x},t)$ reduces to zero in the next iteration.

2.2.3 *Normal damping force*

Normal damping is incorporated to allow energy dissipation of the system upon normal contact. The damping force results in shortened relaxation times and therefore lowers computational costs for simulations approaching mechanical equilibrium. The damping force is given by

$$\mathbf{F}_d(y,x) = \begin{cases} -\beta_d\left(\frac{\mathbf{v}(\mathbf{y},\mathbf{x},t)}{|\mathbf{v}(\mathbf{y},\mathbf{x},t)|}\cdot\mathbf{e}(\mathbf{y},\mathbf{x},t)\right)\mathbf{e}(\mathbf{y},\mathbf{x},t)V_{\mathbf{x}}V_{\mathbf{y}}, \\ \qquad \text{if } |\mathbf{p}(\mathbf{y},t)-\mathbf{p}(\mathbf{x},t)| < R_c \\ 0, \quad \text{otherwise} \end{cases} \tag{6}$$

where β_d is the damping coefficient given by $\beta_d = 2r_d\sqrt{\frac{K_n\rho}{V_{\mathbf{y}}}}$ and $r_d \in [0,1]$ is the damping ratio.

2.2.4 *Self-contact*

The presence of a peridynamic bond between two material points from the same parent particle provides the necessary repulsive force to ensure that the points do not overlap numerically. However, such repulsive forces are absent when the peridynamic bond between the points is broken. Therefore, we specify a self-contact law between nodes of the same parent particle which are not connected by a peridynamic bond but are close to each other due to large deformations. This is especially important for preventing the numerical inter-penetration of different parts of nonconvex particle shapes, and for modeling the contact between various broken segments of a parent particle where a peridynamic force is absent.

Our self-contact law depends on the distance between nodes in the reference (undeformed) configuration. If there is no peridynamic bond between two nodes $\mathbf{x}$ and $\mathbf{y}$ from the same parent particle D_i at time t and the current distance between them is within R_c (i.e. if $|\boldsymbol{\xi}+\boldsymbol{\eta}| < R_c$), the normal repulsive force on $\mathbf{x}$ due to $\mathbf{y}$ is given by

$$\mathbf{f}_r^{\text{self}}(\mathbf{x},\mathbf{y},t) = \begin{cases} c_w \frac{|\boldsymbol{\xi}+\boldsymbol{\eta}|-|\boldsymbol{\xi}|}{|\boldsymbol{\xi}|} \frac{\boldsymbol{\xi}+\boldsymbol{\eta}}{|\boldsymbol{\xi}+\boldsymbol{\eta}|} \chi_{\{|\boldsymbol{\xi}+\boldsymbol{\eta}|<|\boldsymbol{\xi}|\}}, & \text{if } |\boldsymbol{\xi}| < R_c \\ c_w \frac{|\boldsymbol{\xi}+\boldsymbol{\eta}|-R_c}{R_c} \frac{\boldsymbol{\xi}+\boldsymbol{\eta}}{|\boldsymbol{\xi}+\boldsymbol{\eta}|} \chi_{\{|\boldsymbol{\xi}+\boldsymbol{\eta}|<R_c\}}, & \text{if } R_c < |\boldsymbol{\xi}|, \end{cases}$$

where χ_S is the characteristic function of the set S. Damping and friction forces between nodes from the same parent particle in the absence of peridynamic bonds can be defined similar to Equation (4) and Equation (6), respectively.

Note that in the small reference length scale $|\boldsymbol{\xi}| < R_c < \epsilon$, the repulsive contact force is modeled using a repulsive-only peridynamic bond force. This ensures that two nodes with reference distance $|\boldsymbol{\xi}| < R_c$ do not experience any repulsive force from each other unless they come closer than their reference distance $|\boldsymbol{\xi}|$. In large reference length scale $|\boldsymbol{\xi}| > R_c$, the contact force between nodes from the same parent particle is same as the contact force between nodes from different parent particles if $\frac{c_w}{R_c} = K_n$.

2.2.5 *Wall forces*

The wall containing particle aggregates is considered to be rigid (i.e., not deformable) and of thickness at least $\frac{R_c}{2}$. The inner boundary of the container wall is assumed to be rectangular, consisting of straight lines. The point $\mathbf{p}(\mathbf{x},t)$ inside the particle $D_k(t)$ experiences contact force due the wall if the perpendicular distance from $\mathbf{p}(\mathbf{x},t)$ to any wall inner boundary l is smaller than the contact radius R_c. In this case, the repulsive force due to the wall on $\mathbf{p}(\mathbf{x},t)$ is given by

$$\mathbf{F}_r^l(\mathbf{x},t) = \begin{cases} -K_n(R_c - |\mathbf{c}_l(\mathbf{x},t)-\mathbf{p}(\mathbf{x},t)|)V_{\mathbf{x}}\,|S_l(\mathbf{x},t)|\,\mathbf{e}^l(\mathbf{x},t), & \text{if } d_l(\mathbf{x},t) < R_c \\ 0 \quad \text{otherwise}, \end{cases} \tag{7}$$

where $|S_l(\mathbf{x},t)|$ is the volume of the circular segment $S_l(\mathbf{x},t)$ of the ball $B_{R_c}(\mathbf{p}(\mathbf{x},t)$ intersected with l, $\mathbf{c}_l(\mathbf{x},t)$ is the centroid of $S_l(\mathbf{x},t)$, and $d_l(\mathbf{x},t)$ is the distance from $\mathbf{p}(\mathbf{x},t)$ to l (see Figure 1a). Here, $\mathbf{e}_l(\mathbf{x},t)$ is the unit vector in the direction $\mathbf{c}_l(\mathbf{x},t)$ from $\mathbf{p}(\mathbf{x},t)$ given by $\mathbf{e}_l(\mathbf{x},t) = \frac{\mathbf{c}_l(\mathbf{x},t)-\mathbf{p}(\mathbf{x},t)}{|\mathbf{c}_l(\mathbf{x},t)-\mathbf{p}(\mathbf{x},t)|}$ and determines the direction of repulsive wall force on $\mathbf{p}(\mathbf{x},t)$.

In case the point $\mathbf{p}(\mathbf{x},t)$ experiences contact from two different inner wall boundary segments l_i and l_j (e.g. when $\mathbf{p}(\mathbf{x},t)$ is sufficiently close the a corner of a rectangular container, see Figure 1b), the repulsive force on $\mathbf{p}(\mathbf{x},t)$ due to the wall is given by the inclusion-exclusion principle $\mathbf{F}_r^{l_i\cup l_j}(\mathbf{x},t) = \mathbf{F}_r^{l_i}(\mathbf{x},t) + \mathbf{F}_r^{l_j}(\mathbf{x},t) - \mathbf{F}_r^{l_i,l_j}(\mathbf{x},t)$, where

$$\mathbf{F}_r^{l_i,l_j}(\mathbf{x},t) = -K_n(R_c - \left|\mathbf{c}_{l_i,l_j}(\mathbf{x},t)-\mathbf{p}(\mathbf{x},t)\right|)V_{\mathbf{x}}\left|S_{l_i,l_j}(\mathbf{x},t)\right|\mathbf{e}_{l_i,l_j}(\mathbf{x},t),$$

where $S_{l_i,l_j} = S_{l_i} \cap S_{l_j}$, $\mathbf{c}_{l_i,l_j}(\mathbf{x},t)$ is the centroid of S_{l_i,l_j}, and $\mathbf{e}_{l_i,l_j}(\mathbf{x},t) = \frac{\mathbf{c}_{l_i,l_j}(\mathbf{x},t)-\mathbf{p}(\mathbf{x},t)}{\left|\mathbf{c}_{l_i,l_j}(\mathbf{x},t)-\mathbf{p}(\mathbf{x},t)\right|}$. Therefore, for a rectangular wall boundary with straight line segments $\{l_i\}_{i=1}^4$, the repulsive contact force due to the wall boundary is given by

$$\mathbf{F}_r^{\text{wall}}(\mathbf{x},t) = \sum_{i=1}^{4}\mathbf{F}_r^{l_i}(\mathbf{x},t) - \sum_{i<j}\mathbf{F}_r^{l_i,l_j}(\mathbf{x},t). \tag{8}$$

The total friction and damping forces $\mathbf{F}_f^{\text{wall}}(\mathbf{x},t)$ and $\mathbf{F}_d^{\text{wall}}(\mathbf{x},t)$ due to the wall boundary can be computed accordingly from Equation (4) and Equation (6), respectively, by replacing $\mathbf{e}(\mathbf{y},\mathbf{x},t)$ by $\mathbf{e}^l(\mathbf{x},t)$, $V_{\mathbf{y}}$ by $|S_l(\mathbf{x},t)|$, and $\mathbf{p}(\mathbf{y},t)$ by $\mathbf{c}_l(\mathbf{x},t)$.

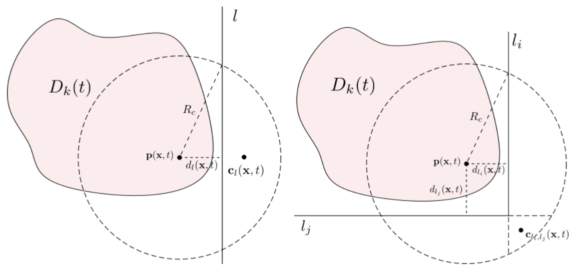

(a) (b)

Fig. 1: Computation of wall contact volume and the centroid of wall volume responsible for exerting contact forces for contact with (a) single and (b) double wall boundaries. The contact radius is exaggerated to show the quantities of interest.

2.2.6 *Combined model*

The equation of motion for the particle aggregate can now be given explicitly. Summing all forces acting on $\mathbf{x}$, the equation of motion of the points $\mathbf{p}(\mathbf{x}, t) \in D_i(t)$, $i = 1, \dots, N$ is given by

$$
\begin{aligned}
&\rho(\mathbf{x})\ddot{\mathbf{u}}(\mathbf{x}, t) = \mathbf{F}(\mathbf{x}, t) + \mathbf{b}(\mathbf{x}, t) \text{ where,} \\
&\mathbf{F}(t, \mathbf{x}) = \\
&\int\limits_{H_\epsilon(\mathbf{x}) \cap D_i(0)} \left(\mathbf{f} + \mathbf{f}_r^{\text{self}} + \mathbf{f}_d^{\text{self}} + \mathbf{f}_f^{\text{self}}\right)(\mathbf{x}', \mathbf{x}, t) dV_{\mathbf{x}'} \\
&+ \sum_{j \neq i} \int\limits_{D_j(0) \cap \{\mathbf{y} : |\mathbf{p}(\mathbf{y}) - \mathbf{p}(\mathbf{x})| < R_c\}} (\mathbf{f}_r + \mathbf{f}_d + \mathbf{f}_f)(\mathbf{y}, \mathbf{x}, t) dV_{\mathbf{y}} \\
&+ \mathbf{F}_r^{\text{wall}}(\mathbf{x}, t) + \mathbf{F}_d^{\text{wall}}(\mathbf{x}, t) + \mathbf{F}_f^{\text{wall}}(\mathbf{x}, t)
\end{aligned}
$$

for $\mathbf{x} \in D_i(0), i = 1, \dots, N$, where $\mathbf{f}_r = \frac{\mathbf{F}_r}{V_{\mathbf{x}}}$, $\mathbf{f}_d = \frac{\mathbf{F}_d}{V_{\mathbf{x}}}$, and $\mathbf{f}_f = \frac{\mathbf{F}_f}{V_{\mathbf{x}}}$ are the repulsive, damping, and friction force density functions, respectively, and they all have the unit of force/volume^2. Here the wall forces are expressed as the body forces $\mathbf{F}_r^{\text{wall}}(\mathbf{x}, t)$, $\mathbf{F}_d^{\text{wall}}(\mathbf{x}, t)$, and $\mathbf{F}_f^{\text{wall}}(\mathbf{x}, t)$ with units of force/volume. This equation of motion is adequate for particle settling problems. In the next section we introduce a complete and time-discretized dynamics to describe the vehicle transport problem. To do this we add the wheel to the dynamics where a prescribed angular velocity or slip is imposed on the wheel.

3 NUMERICAL IMPLEMENTATION

Here, we treat the wheel as a peridynamic domain where the motion is restricted. In this section we outline the main features of the numerical implementation of the vehicle transport problem.

3.1 Time-integration

To perform the time-integration, we use the Velocity-Verlet scheme [32] given by

$$
\begin{aligned}
\mathbf{u}(t + \Delta t) &= \mathbf{u}(t) + \Delta t \dot{\mathbf{u}}(t) + \frac{\Delta t^2}{2} \ddot{\mathbf{u}}(t) \\
\dot{\mathbf{u}}(t + \Delta t) &= \dot{\mathbf{u}}(t) + \frac{\Delta t}{2} \left(\ddot{\mathbf{u}}(t) + \ddot{\mathbf{u}}(t + \Delta t)\right)
\end{aligned} \tag{9}
$$

where $\mathbf{u}, \dot{\mathbf{u}}$, and $\ddot{\mathbf{u}}$ are the displacement, velocity and the acceleration vectors of the particle nodes and $\Delta t > 0$ is the time step. For the simulations, we have taken $\Delta t = 2$ μs.

3.2 Applying velocity constraints and rigidity

Here, we describe the method of prescribing the angular velocity and the slip ratio of the wheel consistent with the velocity-Verlet scheme. We cancel out the radial deformation of the wheel in both cases to prevent the wheel from expanding in the radial direction due to its inertia.

We allow the wheel W to rotate about its centroid, which is $\mathbf{c}^W(t) = \frac{1}{|W|} \int_W \mathbf{p}(\mathbf{x}, t) d\mathbf{x}$. For any point $\mathbf{x}$ in W at $t = 0$ then $\mathbf{p}(\mathbf{x}, t) = \mathbf{x} + \mathbf{u}(\mathbf{x}, t)$ gives its position at time t. The linear velocity $\mathbf{v}^W(t)$ of the wheel is obtained by averaging the velocities of each spatial node on the wheel and is given by $\mathbf{v}^W(t) = \frac{1}{|W|} \int_W \dot{\mathbf{u}}(\mathbf{x}, t) d\mathbf{x}$. For any $\mathbf{x} \in W$ define the radial vector in the frame of reference centered at $\mathbf{c}^W(t)$ as

$$
\mathbf{r}(\mathbf{x}, t) = \mathbf{p}(\mathbf{x}, t) - \mathbf{c}^W(t)
$$

Let $\hat{\mathbf{t}}(\mathbf{x}, t)$ be the tangential unit vector perpendicular to $\mathbf{r}(\mathbf{x}, t)$. Therefore, with respect to the centroid, the relative velocity $\mathbf{v}(\mathbf{x}, t) := \dot{\mathbf{u}}(\mathbf{x}, t) - \mathbf{v}^W(t)$ for all $\mathbf{x} \in W$ can be decomposed in the radial and tangential directions as

$$
\mathbf{v}(\mathbf{x}, t) = v_t(\mathbf{x}, t)\, \widehat{\mathbf{t}}(\mathbf{x}, t) + v_r(\mathbf{x}, t)\, \widehat{\mathbf{r}}(\mathbf{x}, t) \tag{10}
$$

where

$$
\begin{aligned}
v_r(\mathbf{x}, t) &:= |\mathbf{v}(\mathbf{x}, t)| \cos\theta = \langle \mathbf{v}(\mathbf{x}, t), \widehat{\mathbf{r}}(\mathbf{x}, t) \rangle \\
v_t(\mathbf{x}, t) &:= |\mathbf{v}(\mathbf{x}, t)| \sin\theta = \left\langle \mathbf{v}(\mathbf{x}, t), \widehat{\mathbf{t}}(\mathbf{x}, t) \right\rangle
\end{aligned}
$$

where θ is the angle between $\mathbf{v}(\mathbf{x},t)$ and $\widehat{\mathbf{r}}(\mathbf{x},t)$ and $\langle\cdot,\cdot\rangle$ denotes the standard inner product. Alternatively,

$$v_t(\mathbf{x},t) = \mathbf{v}(\mathbf{x},t) - \langle \mathbf{v}(\mathbf{x},t), \mathbf{r}(\mathbf{x},t)\rangle\, \widehat{\mathbf{r}}(\mathbf{x},t).$$

The angular velocity $\omega(\mathbf{x},t)$ of all $\mathbf{x}\in W$ is therefore given by $\omega(\mathbf{x},t) = \frac{v_t(\mathbf{x},t)}{|\mathbf{r}(\mathbf{x},t)|}$. A constant angular velocity ω^{presc} on the wheel is prescribed by setting $\omega(\mathbf{x},t) = \omega^{\text{presc}}$ for all time t for all $\mathbf{x}\in W$. For this case, the linear wheel velocity $\mathbf{v}^W(t)$ is free.

In the peridynamic treatment, the wheel W is deformable, i.e. $\mathbf{u}(\mathbf{x},t)$ is allowed to be non-rigid. In this case, imposing the angular velocity via v_t on all $\mathbf{x}\in W$ implies centrifugal force due to the wheel inertia deforms the wheel in the radial direction. In this article we prevent this, and impose $v_r(\mathbf{x},t) = 0$ for all $\mathbf{x}\in W$. This constraint, together with the prescribed angular velocity constraint, makes the wheel a rigid body, i.e. it undergoes rotations and translations only.

The radius of the wheel is R and the instantaneous longitudinal slip at time t of the wheel is defined as

$$S(t) = -\frac{v_x^W(t) - R\omega^{\text{presc}}}{v_x^W(t)} \tag{11}$$

where $v_x^W(t)$ is the x-component of the linear velocity $\mathbf{v}^W(t)$ of the wheel. A positive value of S implies that the wheel is *slipping* whereas a negative value implies *skidding*. In the fixed slip simulations, both horizontal and angular velocities are fixed, i.e. $v_x^W(\mathbf{x},t) = v_x^{\text{presc}}$ and $\omega(\mathbf{x},t) = \omega^{\text{presc}}$ for all t for all $\mathbf{x}\in W$. This implies $S(t)$ is constant for all t and $v_y^W(t)$ is free. The sinkage is defined as the difference in y-displacement between initial and current position of the wheel.

3.3 Driving force and torque

Let $\mathbf{f}^{\text{dr}}(\mathbf{x},t)$ be the force density acting on $\mathbf{x}\in W$ to maintain the prescribed velocity condition on the wheel. This force imposes a constraint on the deformation $\mathbf{u}(\mathbf{x},t)$ in the W and is derived below. The driving torque density on $\mathbf{x}\in W$ therefore is given by

$$\boldsymbol{\tau}^{\text{dr}}(\mathbf{x},t) = \mathbf{r}(\mathbf{x},t)\times \mathbf{f}^{\text{dr}}(\mathbf{x},t).$$

The total driving force and the total driving torque of the wheel at time t is therefore given by

$$\mathbf{F}^{\text{dr}}(t) = \int_W \mathbf{f}^{\text{dr}}(\mathbf{x},t)dV_{\mathbf{x}}, \tag{12}$$

$$\boldsymbol{\tau}^{\text{dr}}(t) = \int_W \boldsymbol{\tau}^{\text{dr}}(\mathbf{x},t)dV_{\mathbf{x}}, \text{ respectively.} \tag{13}$$

Here we denote $\tau^{\text{dr}}(t) = \left|\boldsymbol{\tau}^{\text{dr}}(t)\right|$.

We now introduce the driving velocity $\mathbf{u}^{dr}(\mathbf{x},t)$ on the wheel. For an imposed angular velocity ω^{presc} the driving velocity is given by

$$\dot{\mathbf{u}}^{\text{dr}}(\mathbf{x},t) = \mathbf{v}^W(t) + \omega^{\text{presc}}\,|\mathbf{r}(\mathbf{x},t)|\,\widehat{\mathbf{t}}(\mathbf{x},t). \tag{14}$$

Alternatively for an imposition of slip specified by ω^{presc} and v_x^{presc} it is given by

$$\dot{\mathbf{u}}^{\text{dr}}(\mathbf{x},t) = v_x^{\text{presc}}\widehat{\mathbf{e}_x} + v_y^W(t)\widehat{\mathbf{e}_y} + \omega^{\text{presc}}\,|\mathbf{r}(\mathbf{x},t)|\,\widehat{\mathbf{t}}(\mathbf{x},t). \tag{15}$$

From the velocity-update equation of the velocity-Verlet scheme (see Equation (9)), the driving force density on $\mathbf{x}\in W$ to maintain the prescribed angular velocity or prescribed slip on the wheel is therefore given by

$$\begin{aligned}&\mathbf{f}^{\text{dr}}(\mathbf{x},t+\Delta t)\\ &= \rho\frac{2}{\Delta t}(\dot{\mathbf{u}}^{\text{dr}}(\mathbf{x},t+\Delta t) - \dot{\mathbf{u}}(\mathbf{x},t+\Delta t)) - \rho\ddot{\mathbf{u}}(\mathbf{x},t+\Delta t).\end{aligned} \tag{16}$$

The time discrete dynamical system of gravel bed and wheel is now described by Equation (16) and

$$\rho\ddot{\mathbf{u}}(\mathbf{x},t) = \mathbf{F}(\mathbf{x},t) - \mathbf{F}^{dr}(\mathbf{x},t) + \mathbf{b}(\mathbf{x},t), \tag{17}$$

for $\mathbf{x}\in W$ and $\mathbf{x}\in D_i(0),\ i = 1,\ldots,N$ and the components of $\mathbf{v}^W(t)$ can be extracted from the dynamics. The combined algorithm is given in Algorithm 1.

4 SIMULATIONS

In this section, we employ numerical experiments to understand how the dynamics of individual grains effect the global dynamics of the gravel bed subject to a wheel rolling over the top of it. We study the dynamics of road beds made with similarly shaped particles.

Algorithm 1 Time integration

Define $\mathbf{u}(\mathbf{x}), \dot{\mathbf{u}}(\mathbf{x}), \ddot{\mathbf{u}}(\mathbf{x}), \mathbf{b}(\mathbf{x})$ for $\mathbf{x} \in D_k$ at time $t = 0$ for $k = 1, 2, \ldots, N$
Compute intra-particle neighbors $S^{\text{ref}}(\mathbf{x}) = \{\mathbf{x}' \in D_k : |\mathbf{x} - \mathbf{x}'| < \epsilon\}$ for all $\mathbf{x} \in D_k$, $k = 1, 2, \ldots, N$
while $t < T$ **do**
  for $k = 1, 2, \ldots, N$ and $\mathbf{x} \in D_k$ **do**
    $\mathbf{u}(\mathbf{x}) \leftarrow \mathbf{u}(\mathbf{x}) + \Delta t \dot{\mathbf{u}}(\mathbf{x}) + \frac{\Delta t^2}{2} \ddot{\mathbf{u}}(\mathbf{x})$ for $\mathbf{x} \in D_k$
    Compute current position $\mathbf{p}(\mathbf{x}) = \mathbf{x} + \mathbf{u}(\mathbf{x})$
  end for
  for $k = 1, 2, \ldots, N$ and $\mathbf{x} \in D_k$ **do**
    Compute inter-particle neighbors $S_j^{\text{nbr}}(\mathbf{x}) = \{\mathbf{y} \in D_j : |\mathbf{p}(\mathbf{x}) - \mathbf{p}(\mathbf{y})| < R_c\}$, $j = 1, 2, \ldots, N$
    Compute peridynamic force density $\mathbf{f}^{\text{peri}}(\mathbf{x}) = \sum\limits_{\mathbf{x}' \in S^{\text{ref}}(\mathbf{x})} \mathbf{f}(\mathbf{x}', \mathbf{x}) V_{\mathbf{x}'}$
    Compute self-contact force density
    $$\mathbf{f}^{\text{self}}(\mathbf{x}) = \sum_{\mathbf{x}' \in S_k^{\text{nbr}}} \Big(\mathbf{f}_r^{\text{self}}(\mathbf{x}', \mathbf{x}) + \mathbf{f}_d^{\text{self}}(\mathbf{x}', \mathbf{x}) + \mathbf{f}_f^{\text{self}}(\mathbf{x}', \mathbf{x}) \Big) V_{\mathbf{x}'}$$
    Compute neighboring-particle force density
    $$\mathbf{f}^{\text{nbr}}(\mathbf{x}) = \sum_{j \neq k} \sum_{\mathbf{y} \in S_j^{\text{nbr}}} (\mathbf{f}_r(\mathbf{y}, \mathbf{x}) + \mathbf{f}_d(\mathbf{y}, \mathbf{x}) + \mathbf{f}_f(\mathbf{y}, \mathbf{x})) V_{\mathbf{y}}$$
    Compute wall-contact force density
    $$\mathbf{f}^{\text{wall}}(\mathbf{x}) = \mathbf{f}_r^{\text{wall}}(\mathbf{y}, \mathbf{x}) + \mathbf{f}_d^{\text{wall}}(\mathbf{y}, \mathbf{x}) + \mathbf{f}_f^{\text{wall}}(\mathbf{y}, \mathbf{x})$$
    Back up acceleration from previous time step: $\ddot{\mathbf{u}}^{\text{old}} := \ddot{\mathbf{u}}(\mathbf{x})$
    $\ddot{\mathbf{u}}(\mathbf{x}) \leftarrow \frac{1}{\rho} \left(\mathbf{f}^{\text{peri}}(\mathbf{x}) + \mathbf{f}^{\text{self}}(\mathbf{x}) + \mathbf{f}^{\text{nbr}}(\mathbf{x}) + \mathbf{f}^{\text{wall}}(\mathbf{x}) + \mathbf{b}(\mathbf{x}, t) \right)$
    if $D_k = W$, the wheel **then**
      Enforce prescribed velocity via driving force $\ddot{\mathbf{u}}(\mathbf{x}) \leftarrow \ddot{\mathbf{u}}(\mathbf{x}) - \frac{1}{\rho} \mathbf{f}^{\text{dr}}(\mathbf{x})$
    end if
    $\dot{\mathbf{u}}(\mathbf{x}) \leftarrow \dot{\mathbf{u}}(\mathbf{x}) + \frac{\Delta t}{2} \left(\ddot{\mathbf{u}}^{\text{old}} + \ddot{\mathbf{u}}(\mathbf{x}) \right)$
  end for
  $t \leftarrow t + \Delta t$
end while

4.1 Simulation setup and initial condition

We consider a rectangular container of dimension 6 m $\times$ 3 m, see Figure 3a. The inner wall boundaries of the container are considered to be rigid. We numerically construct a dry gravel bed in the bottom of the container by first generating a close packing of granular particles over a rigid substrate. We begin by numerically generating a jammed packing of disks within the bottom half of the wall interior. Each disk would then act as a *security disk* for individual particle shape. Next, gravel particle shapes are scaled to fit within the disk boundaries to avoid overlap. The gravel particles are also randomly rotated about their centroids. The particles sizes are further reduced by an amount of $\frac{R_c}{2}$ so that contact forces are not activated at the initial time step of the simulation. The distribution of the security disks in the jammed packing and their centroids are generated from an irregular triangular mesh of the wall interior to introduce polydispersity in the gravel size distribution as well as to avoid crystallization when settling. Here, we consider a gravel bed of 3796 particles. The particle size distribution considered here ranges from 5 mm to 23 mm with mean 16.3 mm and standard deviation 1 mm and follows a skew normal distribution with negative skewness. The packing ratio of the security disks in the distribution is $\phi = 0.45$.

Once the initial gravel aggregate configuration has been generated on top the rigid surface the particles are allowed to settle under a gravitational acceleration of -10 m/s^2 for 20000 time steps, during which the gravel arrangement comes to an equilibrium. Once the particle bed settles, a wheel of radius $R = 0.355$ m is placed at an R_c height above the maximum particle bed height. The initial wheel position is chosen to be away from the left wall by $3R + R_c$, i.e., at $x = -1.923$ m. The wheel is then allowed to settle under gravity on the particle bed for an additional 20000 time steps before a constant angular velocity of -5 rad/s is prescribed. The horizontal displacement and the slip of the wheel is recorded for particle beds consisting of various shapes. The arrangement of security disks containing individual particles is taken to be the same across all shapes. The numerical time step length is taken to be $\Delta t = 10^{-5}$ s.

4.2 Gravel particle shapes

We consider aggregates consisting of gravel particle shapes that are ring-shaped, plus-shaped, and square-shaped (see Figure 2). The particle shapes are chosen to study the effect of nonconvexity, symmetry, and particle topology. The ring-shaped particles are rotationally symmetric, the square-shaped and plus-shaped particles have dihedral symmetry. On the other hand, the plus-shaped particles are nonconvex, whereas the ring-shaped particles are nonconvex with a convex outer boundary. These shapes provide a range of geometric and topological properties that influence the bulk behavior [33, 34, 20]. The surface area of individual particles in terms of their geometric parameters are given in table 2. The *roundness* of the plus-shaped particle is denoted by $c = r/R$ and the *thinness* of the ring-shaped particle is denoted by

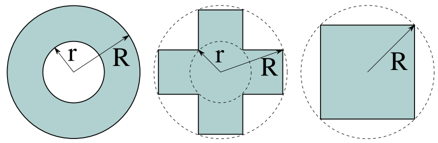

(a) (b) (c)

Fig. 2: Gravel shapes considered: (a) annular or ring-shaped (b) plus-shaped and (c) square-shaped. All shapes are inscribed in security disks.

$\gamma = r/R$ (see fig. 2). For the plus-shaped particles, the roundness is taken to be $c = 0.4$ and the thinness of the ring-shaped particles is taken to be $\gamma = 0.6$.

Table 2: Surface area of individual particles and the bulk volume fraction at equilibrium.

Shape	Annulus	Plus	Square
Particle volume	$\pi R^2(1-\gamma^2)$	$c^2R^2(1+4\sqrt{\frac{2}{c^2}-1})$	$2R^2$

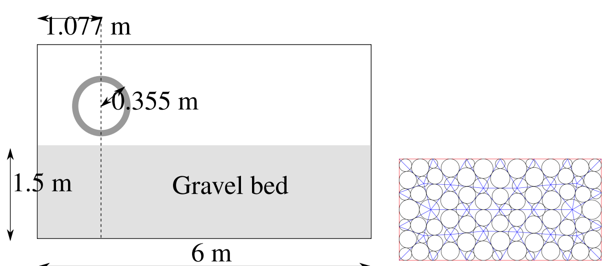

(a) (b)

Fig. 3: (a) Schematics of the simulation setup (b) An example of a jammed disk configuration generated from a triangular mesh of a given particle bulk boundary.

4.2.1 Effect of gravel shape on mobility

In this section, the angular velocity is fixed and the gravel does not damage. The effect of gravel shape on the horizontal displacement, velocity, and slip of the wheel is shown in Figures 4 and 5. We observe that the fastest horizontal *transit* speed over the road bed is achieved with gravel shapes that give the least slip. Among the shapes considered, the gravel bed consisting of square-shaped particles give the slowest transit speed with the most amount of slip. While road beds made with ring-shaped gravel particles show the least amount of slip. More generally, for any particle shape the simulations show that wheel slip is caused by the displacement of gravel particles at the contact point of the wheel with the gravel bed, and by the collapse of particle columns that carry the weight of the wheel.

The nonzero angular velocity is prescribed on the wheel only after it settles to an equilibrium height on the road bed. An initial jump in the slip ratio is observed near this time (0.2 - 0.4 μs) as the linear velocity of wheel is small (see Figure 4c). For $t > 0.5$ μs the wheel motion stabilizes and the slip ratio is the highest for the square-shaped gravel particles and is the lowest for the ring-shaped gravel particles. Snapshots of simulations are shown in Figures 6 and 7. Compared to simulations without fracture (on the left panel), we see less sinkage in the simulations with fracture. This is especially notable for the square-shaped particles (see Figures 6c and 7c).

4.3 Effect of gravel inertia

Due to the frictional contact between the wheel and the surface of the gravel aggregate, the gravel particles near the contact region are displaced, leading to wheel slip. Simulations show that the inertia of the gravel particles play an important role in top-layer gravel displacement. To study the effect of gravel inertia, we consider ring-shaped particles with annuli of different thinness. Maintaining a constant outer radius R, the inner radius is taken to be γR, where $\gamma = 0.4, 0.5, 0.6$, and 0.7. Increasing the inner ratio implies that for a fixed outer radius, the mass of the ring decreases. The mean horizontal velocity of the wheel (see Figure 8) is observed to be a decreasing function of γ. Also, the slip of the wheel is increases with γ.

Now we calculate the total energy $E(L)$ consumed by the wheel to travel a fixed horizontal distance L. To do this let $\tau(t)$ be the driving torque, $\theta(t)$ be the angular displacement of the wheel at time t, and $\omega = \frac{d\theta}{dt}$ be the angular velocity of the wheel. Starting at time t_0, let t_1 be the time when the wheel reaches a horizontal distance of L. When the angular velocity is held constant and prescribed, the energy required to move the wheel a distance L is given by

$$\begin{aligned} E(L) &= \int_{t_0}^{t_1} \tau^{\mathrm{dr}}(t)d\theta(t) + \int_{t_0}^{t_1} \mathbf{F}^{\mathrm{dr}}(t)\cdot d\mathbf{u}(t) \\ &= \int_{t_0}^{t_1} \tau^{\mathrm{dr}}(t)\omega dt + \int_{t_0}^{t_1} F_x^{\mathrm{dr}}(t)v_x(t) + F_y^{\mathrm{dr}}(t)v_y(t)dt, \end{aligned}$$

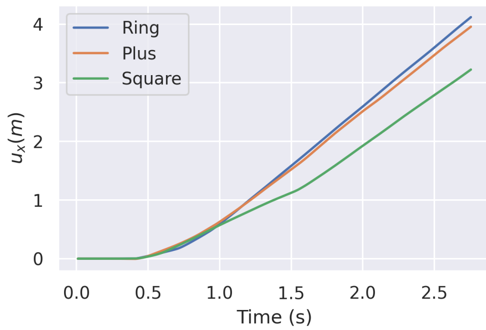

(a)

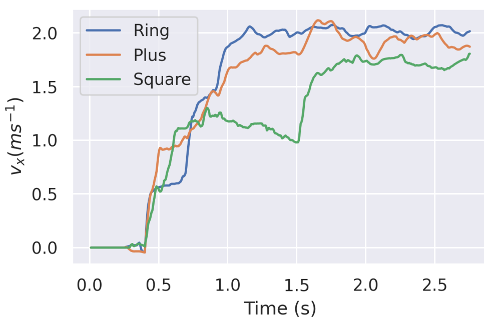

(b)

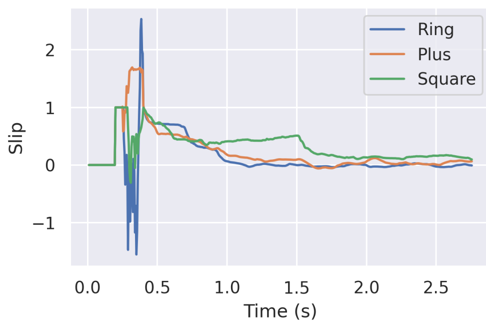

(c)

Fig. 4: Wheel mobility on gravel without fracture: (a) horizontal displacement (b) horizontal velocity and (c) slip of the wheel on particle beds consisting of different shapes in the fixed angular velocity simulations.

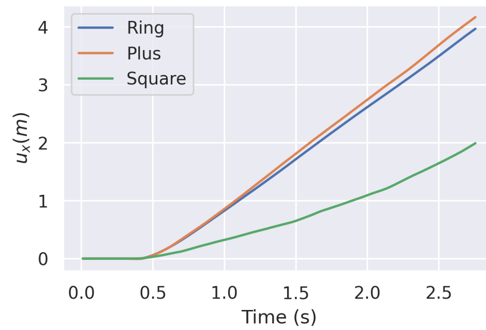

(a)

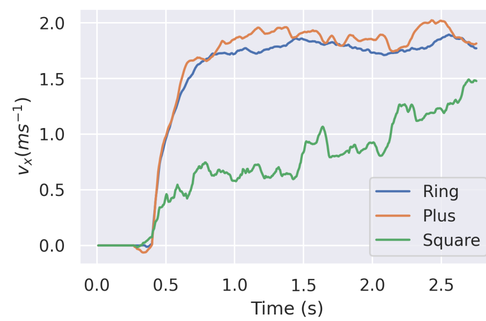

(b)

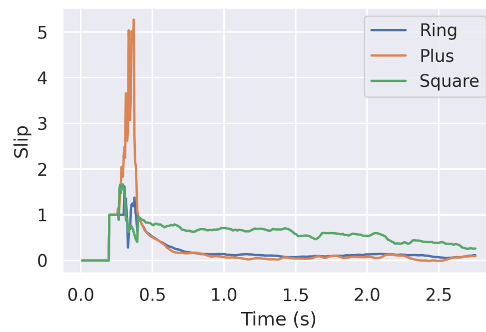

(c)

Fig. 5: Wheel mobility on gravel with fracture: (a) horizontal displacement, (b) horizontal velocity, and (c) slip of the wheel on particle beds consisting of different shapes in the fixed angular velocity simulations.

where $\mathbf{F}^{\mathrm{dr}}$ and τ^{dr} are given by (12). The total energy $E(L)$ consumed by the wheel to travel a horizontal distance of $L = 3$ m is compared for different particle shapes in Figure 9. For gravel particles of all shapes, the energy required to travel the same distance is higher when particles can fracture. Due to low mobility of wheels moving over gravel made up of square shaped particles, the required energy is the highest, both with and without fracture. The energy required for the ring-shaped and the plus-shaped particles is reversed when fracture is possible, this is also reflected in the velocity plots of Figures 4b and 5b.

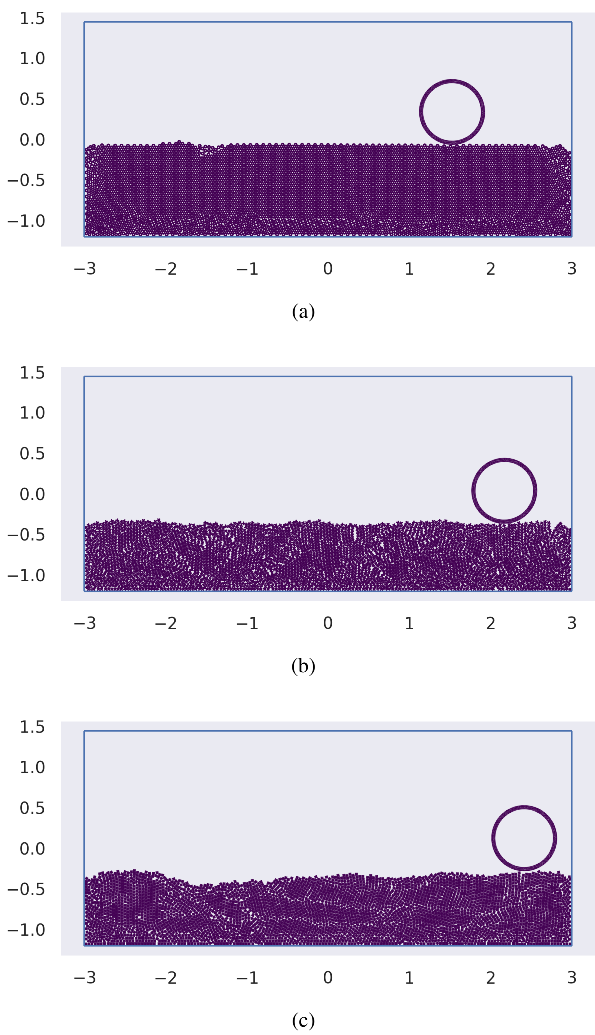

Fig. 6: Snapshots of simulations showing a vehicle wheel moving on gravel beds consisting of (a) ring-shaped, (b) plus-shaped, and (c) square-shaped particles, where gravel damage is turned off.

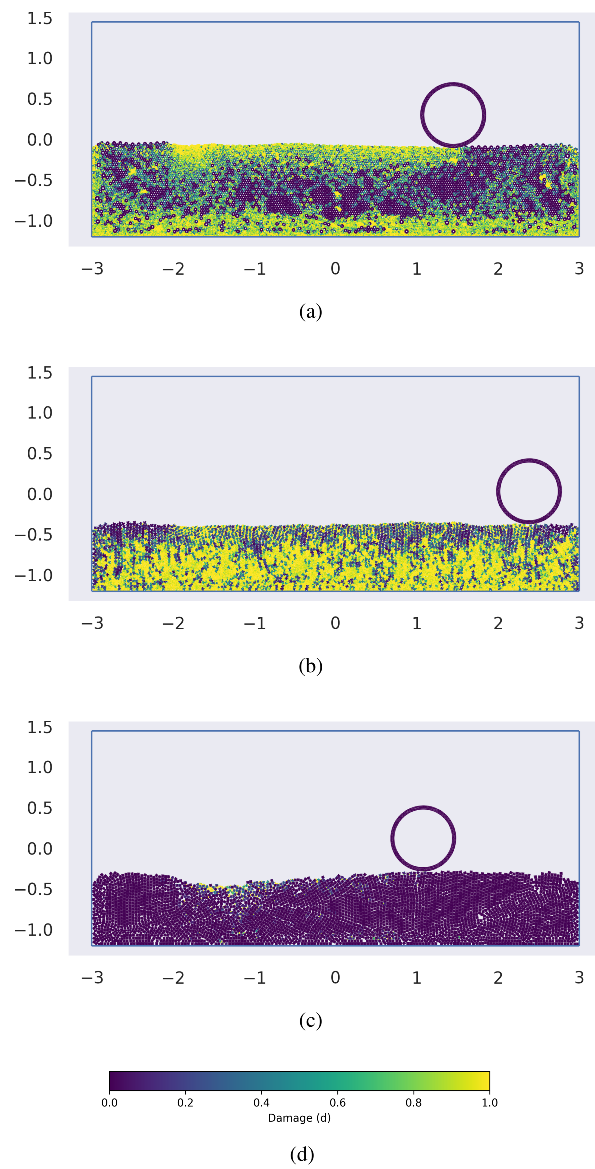

Fig. 7: Snapshots of simulations where gravels are allowed to undergo fracture. Here, gravel beds consist of (a) ring-shaped, (b) plus-shaped, and (c) square-shaped particles. The damage value of each node of each particle is shown in color. The initial contact point between the wheel and the gravel bed (x = -1.9 m) shows significant damage.

4.3.1 Bulk damage due to wheel weight

Here, we consider brittle gravel particles with critical energy release rate $G_c = 135$ J/m^2. The gravel particles fracture using the model described in Section 2.1.

The damage of each gravel particle is defined as the mean damage value of each node (see Section 2.1) in the particle. The bulk damage is defined as the mean damage of all particles present in the aggregate.

When the aggregate settles under its own weight, some damage occurs within the aggregate. Higher damage values are seen toward the bottom of the settled aggregate due to the weight of the particle columns (Figure 7). At the site of the first contact between the wheel and the gravel bed (i.e. at $x = -1.923$ m), a larger value of damage is seen. This is due to increased momentum the impact of the wheel falling from the height R_c. When the wheel rolls on the gravel surface, wheel weight and gravel-to-gravel frictional contact causes additional dam-

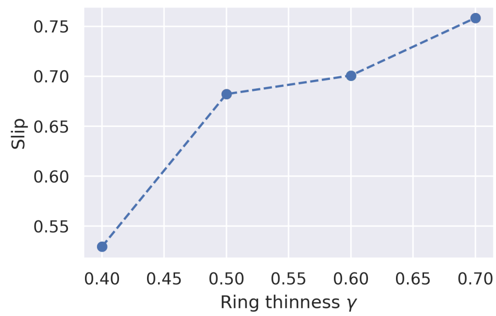

Fig. 8: Average wheel slip with respect to ring thinness γ. In the fixed angular velocity simulations, the wheel slip increases and the horizontal wheel velocity decreases as the inner radii of the ring-shaped gravel is increased.

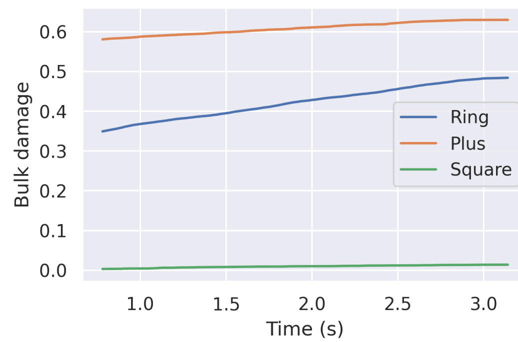

(a)

Fig. 10: Bulk damage of the gravel aggregate with respect to time.

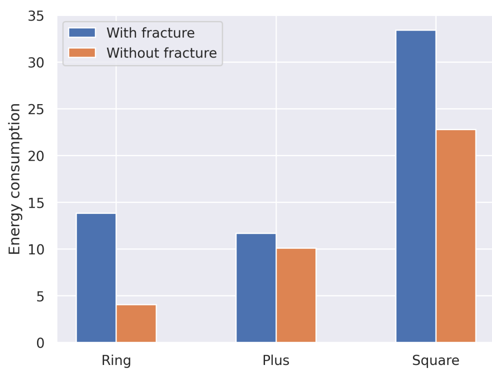

Fig. 9: Energy required to drive the wheel to a horizontal distance of 3 m at a constant angular velocity

age near the surface of the gravel bed.

The bulk damage for aggregates consisting of various shapes is shown in Figure 10. After setting, the plus-shaped particles go through the most amount of initial damage due to the weight of the particle columns, but after doing so become more resistant to the weight of the wheel. As the wheel starts rolling on the gravel bed, the rate of bulk damage is the highest for the ring-shaped particles, whereas it is the lowest for the square-shaped particles.

4.4 Fixed slip simulations

In the following simulations we will prescribe a fixed slip ratio for the wheel. This is achieved by prescribing both the angular and the horizontal velocity of wheel at each time step of the simulation as described in Section 3.2. Such constraints are easy to impose in a laboratory setup, where the longitudinal and angular velocities are controlled using a carriage moving on parallel rails or a DC motor, respectively [35]. For the wheel radius $R = 0.355$ and fixed angular velocity $\omega = 5$ rad/s, we consider horizontal velocities such that the slip (as defined by (11)) is $S = 0, 0.3, 0.5,$ and 0.7. The corresponding horizontal velocities are computed using the formula $v_x = |\omega| R(1 - S)$. To produce multiple simulation results in a reasonable time, we have reduced the number of gravel particles in the simulation by increasing the mean particle size of the distribution. As a result, all simulations in this section consists of 859 particles with mean radius 40 mm and standard deviation 4 mm.

4.4.1 *Shape-effect of driving torque in fixed-slip simulations*

The plot for driving torque versus the slip on aggregates consisting of ring-shaped, plus-shaped, and square-shaped particles are shown in Figure 11. For these simulations the thinness of the rings is taken to be $\gamma = 0.7$. The driving torque follows a monotonically increasing trend in slip and follows the characteristic of the experimentally observed simulations for all particle shapes as in [35]. For nonnegative slip, the driving torque on aggregates made of square-shaped, plus-shaped, and ring-shaped gravel particles are in the increasing order, which is similar to the energy consumption without fracture Figure 9.

5 CONCLUSION

In this work, we provide a computational platform with stable implementation for simulations of a vehicle wheel rolling over gravel beds, where the different gravel particle geometry, topology, deformablity, and fracture toughness are accommodated. Comparison of

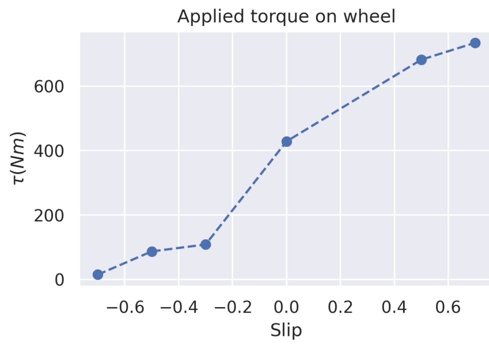

(a)

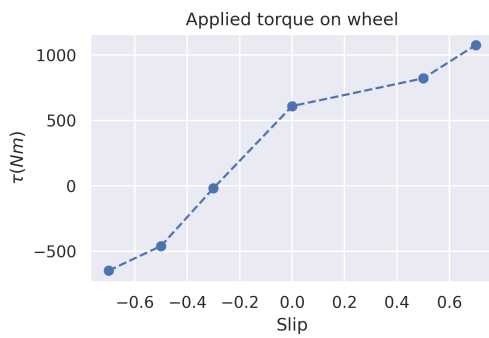

(b)

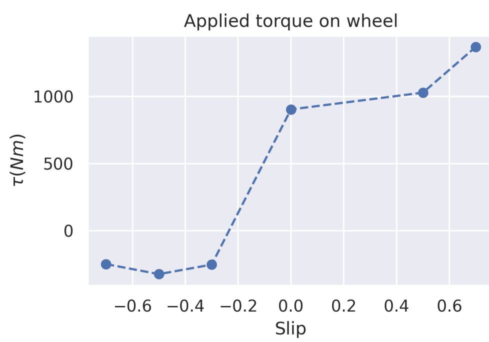

(c)

Fig. 11: Driving torque vs slip in fixed-slip simulations for gravel shapes (a) ring (b) plus (c) square

dynamic vehicle mobility measures including longitudinal displacement, velocity, and slip for transit over particle beds consisting of different gravel geometries and topologies are carried out. We conclude by summarizing our findings below.

The effect of gravel shape on the horizontal displacement, velocity, and slip of the wheel is investigated through numerical simulation. The fastest horizontal transit speed over the gravel bed is achieved with gravel shapes that give the least slip. The gravel bed consisting of square-shaped particles give the slowest transit speed with the most amount of slip, while gravel beds made with ring-shaped gravel particles show the least amount of slip. More generally, for any particle shape the simulations show that wheel slip is caused by the displacement of gravel particles at the contact point of the wheel with the gravel bed, and by the collapse of particle columns that carry the weight of the wheel. When compared to simulations without fracture, one sees less sinkage across all shapes in the simulations with fracture. This is especially notable for the square-shaped particles (see Figures 6c and 7c).

The effect of gravel particle geometry on the overall energy needed to travel a prescribed distance is investigated. Due to low mobility of wheels moving over gravel made up of square shaped particles, the required energy is the highest, both with and without fracture. It is found that the energy required to travel the same distance is higher when particles can fracture. This is in line with the fact that energy is absorbed by the fracture process. Interestingly the energy required for the ring-shaped and the plus-shaped particles is reversed when fracture is possible.

Particle geometry and topology effects particle damage consequently influencing macroscopic transport properties. Here, simulations show the plus-shaped particles go through the most amount of initial damage due to the weight of the particle columns, but after doing so become more resistant to the weight of the wheel. This is due to broken shards filling the interstitial space between intact particles. As the wheel starts rolling on the gravel bed, the rate of bulk damage is the highest for the ring-shaped particles, whereas it is the lowest for the square-shaped particles.

Last, our simulations show that the driving torque exhibits a monotonically increasing trend with increasing slip and follows the trend seen in experimentally observed simulations [35].

Work currently under development aims to simulate the full three dimensional gravel bed problem.

5.1 Acknowledgements

This material is based upon work supported by the U. S. Army Research Laboratory and the U. S. Army Research Office under Contract/Grant Number W911NF-19-1-0245. Portions of this research were conducted with high performance computing resources provided by Louisiana State University (http://www.hpc.lsu.edu). The simulations were performed using the open-source soft-

ware [1]`perigrain`, which is based on the PeriDEM methodology.

REFERENCES

[1] Petkevičius, K., Maskeliūnaitė, L., and Sivilevičius, H., 2019, "Determining travel conditions on motorways for automobile transport based on the case study for lithuanian highways," *Transport,* **34**(1), pp. 89–102.

[2] Pasindu, H., Gamage, D., and Bandara, J., 2020, "Framework for selecting pavement type for low volume roads," *Transportation Research Procedia,* **48**, pp. 3924–3938 Recent Advances and Emerging Issues in Transport Research – An Editorial Note for the Selected Proceedings of WCTR 2019 Mumbai.

[3] Diógenes, L. M., Bessa, I. S., Branco, V. T. F. C., and Mahmoud, E., 2019, "The influence of stone crushing processes on aggregate shape properties," *Road Materials and Pavement Design,* **20**(4), pp. 877–894.

[4] Taberlet, N., Morris, S. W., and McElwaine, J. N., 2007, "Washboard road: The dynamics of granular ripples formed by rolling wheels," *Phys. Rev. Lett.,* **99**, Aug, p. 068003.

[5] Žuraulis, V., Sivilevičius, H., Šabanovič, E., Ivanov, V., and Skrickij, V., 2021, "Variability of gravel pavement roughness: An analysis of the impact on vehicle dynamic response and driving comfort," *Applied Sciences,* **11**(16).

[6] Paterson, W. D., and Watanatada, T., 1985, "Relationships between vehicle speed, ride quality, and road roughness,".

[7] Murphy, K. A., Dahmen, K. A., and Jaeger, H. M., 2019, "Transforming Mesoscale Granular Plasticity Through Particle Shape," *Phys. Rev. X,* **9**(1), Jan., p. 011014.

[8] Athanassiadis, A. G., Miskin, M. Z., Kaplan, P., Rodenberg, N., Lee, S. H., Merritt, J., Brown, E., Amend, J., Lipson, H., and Jaeger, H. M., 2014, "Particle shape effects on the stress response of granular packings," *Soft Matter,* **10**(1), pp. 48–59.

[9] Sun, S., Zhu, F., Wei, J., Wang, W., and Le, H., 2019, "Experimental study on shear failure mechanism and the identification of strength characteristics of the soil-rock mixture," *Shock and Vibration,* **2019**.

[10] Yao, Y., Li, J., Ni, J., Liang, C., and Zhang, A., 2022, "Effects of gravel content and shape on shear behaviour of soil-rock mixture: Experiment and dem modelling," *Computers and Geotechnics,* **141**, p. 104476.

[11] Knuth, M. A., Johnson, J., Hopkins, M., Sullivan, R., and Moore, J., 2012, "Discrete element modeling of a mars exploration rover wheel in granular material," *Journal of Terramechanics,* **49**(1), pp. 27–36.

[12] Cundall, P. A., and Strack, O. D. L., 1979, "A discrete numerical model for granular assemblies," *Géotechnique,* **29**(1), Mar., pp. 47–65 Publisher: ICE Publishing.

[13] Kawamoto, R., Andò, E., Viggiani, G., and Andrade, J. E., 2018, "All you need is shape: predicting shear banding in sand with ls-dem," *Journal of the Mechanics and Physics of Solids,* **111**, pp. 375–392.

[14] Harmon, J. M., Arthur, D., and Andrade, J. E., 2020, "Level set splitting in dem for modeling breakage mechanics," *Computer Methods in Applied Mechanics and Engineering,* **365**, p. 112961.

[15] Silling, S. A., 2000, "Reformulation of elasticity theory for discontinuities and long-range forces," *Journal of the Mechanics and Physics of Solids,* **48**(1), Jan., pp. 175–209.

[16] Behzadinasab, M., Vogler, T. J., Peterson, A. M., Rahman, R., and Foster, J. T., 2018, "Peridynamics Modeling of a Shock Wave Perturbation Decay Experiment in Granular Materials with Intra-granular Fracture," *J. dynamic behavior mater.,* **4**(4), Dec., pp. 529–542.

[17] Zhu, F., and Zhao, J., 2019, "Modeling continuous grain crushing in granular media: A hybrid peridynamics and physics engine approach," *Computer Methods in Applied Mechanics and Engineering,* **348**, May, pp. 334–355.

[18] Zhu, F., and Zhao, J., 2019, "A peridynamic investigation on crushing of sand particles," *Géotechnique,* **69**(6), June, pp. 526–540.

[19] Jha, P. K., Desai, P. S., Bhattacharya, D., and Lipton, R., 2021, "Peridynamics-based discrete element method (PeriDEM) model of granular systems involving breakage of arbitrarily shaped particles," *Journal of the Mechanics and Physics of Solids,* **151**, June, p. 104376.

[20] Ludewig, F., and Vandewalle, N., 2012, "Strong interlocking of nonconvex particles in random packings," *Phys. Rev. E,* **85**, May, p. 051307.

[21] Recuero, A., Serban, R., Peterson, B., Sugiyama, H., Jayakumar, P., and Negrut, D., 2017, "A high-fidelity approach for vehicle mobility simulation: Nonlinear finite element tires operating on granular material," *Journal of Terramechanics,* **72**, Aug., pp. 39–54.

[1]https://github.com/debdeepbh/perigrain

[22] Recuero, A. M., Contreras, U., Patel, M., and Shabana, A. A., 2016, "ANCF Continuum-Based Soil Plasticity for Wheeled Vehicle Off-Road Mobility," *Journal of Computational and Nonlinear Dynamics,* **11**(4), 01 044504.

[23] Bhattacharya, D., and Lipton, R., 2023, "Simulating grain shape effects and damage in grannular media using peridem," *SIAM Journal on Computing,* **45**(1), pp. B1–B26.

[24] Bobaru, F., Yang, M., Alves, L. F., Silling, S. A., Askari, E., and Xu, J., 2009, "Convergence, adaptive refinement, and scaling in 1d peridynamics," *International Journal for Numerical Methods in Engineering,* **77**(6), pp. 852–877.

[25] Silling, S., and Askari, E., 2005, "A meshfree method based on the peridynamic model of solid mechanics," *Computers & Structures,* **83**(17-18), June, pp. 1526–1535.

[26] Ha, Y. D., and Bobaru, F., 2010, "Studies of dynamic crack propagation and crack branching with peridynamics," *Int J Fract,* **162**(1-2), Mar., pp. 229–244.

[27] Trageser, J., and Seleson, P., 2020, "Bond-Based Peridynamics: a Tale of Two Poisson's Ratios," *J Peridyn Nonlocal Model,* **2**(3), Sept., pp. 278–288.

[28] Silling, S. A., Epton, M., Weckner, O., Xu, J., and Askari, E., 2007, "Peridynamic States and Constitutive Modeling," *J Elasticity,* **88**(2), Aug., pp. 151–184.

[29] Desai, P. S., Mehta, A., Dougherty, P. S., and Higgs, C. F., 2019, "A rheometry based calibration of a first-order DEM model to generate virtual avatars of metal Additive Manufacturing (AM) powders," *Powder Technology,* **342**, Jan., pp. 441–456.

[30] Martins, J., and Oden, J., 1983, "A numerical analysis of a class of problems in elastodynamics with friction," *Computer Methods in Applied Mechanics and Engineering,* **40**(3), pp. 327–360.

[31] Campos, L., Oden, J., and Kikuchi, N., 1982, "A numerical analysis of a class of contact problems with friction in elastostatics," *Computer Methods in Applied Mechanics and Engineering,* **34**(1-3), pp. 821–845.

[32] Hairer, E., Lubich, C., and Wanner, G., 2003, "Geometric numerical integration illustrated by the Störmer–Verlet method," *Acta Numerica,* **12**, May, pp. 399–450 Publisher: Cambridge University Press.

[33] Donev, A., Connelly, R., Stillinger, F. H., and Torquato, S., 2007, "Underconstrained jammed packings of nonspherical hard particles: Ellipses and ellipsoids," *Phys. Rev. E,* **75**, May, p. 051304.

[34] Desmond, K., and Franklin, S. V., 2006, "Jamming of three-dimensional prolate granular materials," *Phys. Rev. E,* **73**, Mar, p. 031306.

[35] Smith, W., Melanz, D., Senatore, C., Iagnemma, K., and Peng, H., 2014, "Comparison of discrete element method and traditional modeling methods for steady-state wheel-terrain interaction of small vehicles," *Journal of Terramechanics,* **56**, Dec., pp. 61–75.